SAND2020-4725C

Towards computational imaging for intelligence in highly scattering aerosols

Brian Z Bentz[a], Brian J. Redman[a], John D. van der Laan[a], Karl Westlake[a], Andrew Glen[a], Andres L. Sanchez[a], and Jeremy B. Wright[a]

[a]Sandia National Laboratories, P.O. Box 5800, Albuquerque, United States

ABSTRACT

Aerosols like fog reduce situational awareness and cause down-time that for critical systems or operations is unacceptable. Information is lost to the random scattering and absorption of light by tiny particles. Computational diffuse optical imaging methods show promise for interpreting the light transmitted or reflected through fog, enabling sensing and imaging to improve situational awareness. Developing this capability first requires verification and validation of diffuse transport models in fog. For this reason, analytical solutions were developed and compared to experimental data captured at the Sandia National Laboratory Fog Chamber facility. The weak angular dependence and diffusion approximations to the radiative transfer equation were found sufficient to predict light propagation in fog under the appropriate conditions.

Keywords: Degraded Visual Environment; Fog; Radiative Transfer; Diffusion Equation

1. INTRODUCTION

Degraded visual environments (DVEs) are a major challenge for security and monitoring systems because situational awareness can be diminished or completely lost, limiting mission effectiveness. When the state of the environment can change in an unknown way it becomes difficult to manage risk and current solutions usually require costly actions. Aerosols that are naturally occurring or man-made can create DVEs that are sufficiently severe to impact security, transportation, aviation, remote sensing, surveillance, and more.[1–5] Fog is particularly concerning because it occurs in all climates and at certain locations with high frequency. Information is scrambled because the propagation direction of light in fog becomes randomized due to scattering from micron sized particles. Moreover, the light will be absorbed, leading to the loss of information. Therefore, an approach to maximize information transfer through fog to improve situational awareness is to decipher the scattered light and minimize the effect of absorption.

One set of such approaches are incoherent methods that do not take advantage of the wave nature of light, and therefore could be insensitive to particle motion in fog. An example incoherent approach is diffuse optical imaging (DOI), which was developed for biomedical applications. DOI methods generally rely on computational imaging to invert a model that describes the propagation of photons in a scattering media.[6] Through optimization techniques,[7,8] it becomes possible to detect objects,[9] estimate the locations of objects[10–12] and even recover the shape of objects.[7,8,13,14] Our goal is to develop a DOI approach for aerosols like fog. DOI methods suffer relatively low spatial resolution because the coherent information is not used. However, for applications related to improving situational awareness and physical security, we expect the resolution of incoherent methods to be sufficient to locate and identify threats. An advantage of DOI is the potential for a ten times enhancement of imaging range in aerosols compared to ballistic approaches that reject scattered light.[1,15]

A first step in developing DOI methods for aerosols is to verify and validate the models of light propagation in fog. To this end, experiments were performed at the Sandia National Laboratory Fog Chamber facility (SNLFC), which can generate a repeatable and well characterized natural fog.[15–19] In Section 2, the light propagation models are described. Analytical solutions are derived to be compared to experimental results. In Section 3, the

Further author information: (Send correspondence to Brian Z. Bentz)
E-mail: bzbentz@sandia.gov
E-mail: fog@sandia.gov

relevant optical parameters of fog and corresponding model simulations are presented. In Section 4, a method used to determine the line of sight of each camera pixel is presented. This measurement model allows comparison of images captured within the fog to model predictions. The experimental setup is described in Section 5 and the results are presented in Section 6.

2. MODELS

2.1 Radiative Transfer Equation

Propagation of electromagnetic waves in scattering media can be described by the radiative transfer equation (RTE)[6]

$$\frac{1}{c}\frac{\partial}{\partial t}I(\mathbf{r},t,\hat{\mathbf{\Omega}}) + \hat{\mathbf{\Omega}}\cdot\nabla I(\mathbf{r},t,\hat{\mathbf{\Omega}}) + (\mu_a+\mu_s)I(\mathbf{r},t,\hat{\mathbf{\Omega}}) = \mu_s\int_{4\pi} d\hat{\mathbf{\Omega}}' f(\hat{\mathbf{\Omega}}'\to\hat{\mathbf{\Omega}})I(\mathbf{r},t,\hat{\mathbf{\Omega}}) + Q(\mathbf{r},t,\hat{\mathbf{\Omega}}) \tag{1}$$

where $\mathbf{r}$ denotes the position, c is the speed of light in the medium, $I(\mathbf{r},t,\hat{\mathbf{\Omega}})$ (W/m^2/s/sr) is the radiance at time t in direction $\hat{\mathbf{\Omega}}$, $\mu_a = \sigma_a n$ (m^{-1}) is the absorption coefficient, $\mu_s = \sigma_s n$ is the scattering coefficient (m^{-1}), σ_a is the absorption cross section (m^2), σ_s is the scattering cross section (m^2), n is the particle density (cm^{-3}), $l = 1/(\mu_s+\mu_a)$ is the mean free path, $f(\hat{\mathbf{\Omega}}'\to\hat{\mathbf{\Omega}})$ is the scattering phase function from incidence direction $\hat{\mathbf{\Omega}}'$ to scattering direction $\hat{\mathbf{\Omega}}$, and $Q(\mathbf{r},t,\hat{\mathbf{\Omega}})$ (W/m^3/s/sr) is the radiance source term. The RTE provides an incoherent model that treats light as particles undergoing elastic collisions within a medium where interference effects are assumed to average to zero. Integrating over solid angle results in a continuity equation

$$\frac{1}{c}\frac{\partial}{\partial t}\phi(\mathbf{r},t) + \nabla\cdot\mathbf{J}(\mathbf{r},t) + \mu_a\phi(\mathbf{r},t) = S(\mathbf{r},t) \tag{2}$$

where $\phi(\mathbf{r},t) = \int_{4\pi} d\hat{\mathbf{\Omega}} I(\mathbf{r},t,\hat{\mathbf{\Omega}})$ is the fluence rate (W/m^2/s), $\mathbf{J}(\mathbf{r},t) = \int_{4\pi} d\hat{\mathbf{\Omega}}\hat{\mathbf{\Omega}} I(\mathbf{r},t,\hat{\mathbf{\Omega}})$ is the flux density (W/m^2/s), and $S(\mathbf{r},t) = \int_{4\pi} d\hat{\mathbf{\Omega}} Q(\mathbf{r},t,\hat{\mathbf{\Omega}})$ is the source (W/m^3/s).

2.2 Diffusion Equation

We can assume the radiance is linearly anisotropic with weak angular dependence and expand to first order in $\hat{\mathbf{\Omega}}$[20,21]

$$I(\mathbf{r},t,\hat{\mathbf{\Omega}}) = \frac{1}{4\pi}\phi(\mathbf{r},t) + \frac{3}{4\pi}\mathbf{J}(\mathbf{r},t)\cdot\hat{\mathbf{\Omega}}. \tag{3}$$

Furthermore, assuming an isotropic source and that the rate of time variation in $\mathbf{J}$ is much slower than the collision frequency, it possible to relate the flux density to the fluence rate, resulting in Fick's law[22]

$$\mathbf{J}(\mathbf{r},t) = -D\Delta\phi(\mathbf{r},t), \tag{4}$$

where the diffusion coefficient $D = 1/[3(\mu_s'+\mu_a)]$, $\mu_s' = \mu_s(1-g)$ is the reduced scattering coefficient, g is the average cosine of the scattering angle, or the anisotropy parameter, and $l^* = 1/(\mu_s'+\mu_a)$ is the transport mean free path. As g decreases from 1, the light becomes less forward scattered, 0 implies isotropic scatter, and negative values imply backwards scattering. Plugging (4) into (2), the result is the diffusion equation (DE)

$$\frac{1}{v}\frac{\partial}{\partial t}\phi(\mathbf{r},t) - \nabla\cdot[D(\mathbf{r})\nabla\phi(\mathbf{r},t)] + \mu_a(\mathbf{r})\phi(\mathbf{r},t) = S(\mathbf{r},t). \tag{5}$$

It has been found that the weak angular dependence assumption (3) can be invalid when μ_a is large relative to μ_s and near boundaries and sources.[21] The solution to the DE is

$$\phi(\mathbf{r},t) = \int g(\mathbf{r},\mathbf{r}',t) * S(\mathbf{r}',t)d\mathbf{r}', \tag{6}$$

where $g(\mathbf{r}, \mathbf{r}', t)$ is a Green's function to be determined and $*$ signifies a temporal convolution. If the medium is homogeneous with constant D and μ_a, and $S(\mathbf{r}', t) = S_o \delta(\mathbf{r}_s, t)$, where $\mathbf{r}_s$ is the location of a point source with power S_o (W) and δ is the Dirac delta function, the temporal analytic Green's function solution to the DE is[23]

$$\phi(\mathbf{r}, t) = \frac{S_o c}{(4\pi D c t)^{3/2}} \exp\left(\frac{-|\mathbf{r} - \mathbf{r}_s|^2}{4Dct} - \mu_a c t\right). \tag{7}$$

Solving for $\mathbf{J}$ using (4) gives

$$\mathbf{J}(\mathbf{r}, t) = \frac{S_o \mathbf{r}}{16(\pi D c)^{3/2} t^{5/2}} \exp\left(\frac{-|\mathbf{r} - \mathbf{r}_s|^2}{4Dct} - \mu_a c t\right). \tag{8}$$

Taking the Fourier transform of (5) with $\exp(j\omega t)$ time dependence results in the frequency domain form of the DE

$$\nabla \cdot [D(\mathbf{r}) \nabla \phi(\mathbf{r}, \omega)] - [\mu_a(\mathbf{r}) + j\omega/c]\, \phi(\mathbf{r}, \omega) = -S(\mathbf{r}; \omega), \tag{9}$$

where the fluence rate $\phi(\mathbf{r}, \omega)$ has units of W/m^2. Within a homogeneous medium and far from the light source, (9) simplifies to a scalar wave equation

$$\nabla^2 \phi(\mathbf{r}, \omega) + k^2 \phi(\mathbf{r}, \omega) = 0, \tag{10}$$

where $k^2 = (-\mu_a c - j\omega)/(Dc)$ is the wave number squared, and the solution,

$$\phi(\mathbf{r}, \omega) = \left(\frac{S_o}{4\pi D}\right) \frac{\exp\left(-jk|\mathbf{r} - \mathbf{r}_s|\right)}{|\mathbf{r} - \mathbf{r}_s|}, \tag{11}$$

is the temporal Fourier transform of (7) and describes the propagation of what have been called diffuse photon density waves (DPDW's).[24] The modulation frequency ω is on the order of MHz, and for the case of continuous wave or unmodulated ($\omega = 0$) light, (11) simplifies to

$$\phi(\mathbf{r}) = \left(\frac{S_o}{4\pi D}\right) \frac{\exp\left(\sqrt{\frac{\mu_a}{D}}|\mathbf{r} - \mathbf{r}_s|\right)}{|\mathbf{r} - \mathbf{r}_s|}. \tag{12}$$

Again, solving for $\mathbf{J}$ using (4) gives

$$\mathbf{J}(\mathbf{r}) = \left[\frac{S_o(\mathbf{r} - \mathbf{r}_s)}{4\pi}\right] \left(\frac{-\sqrt{\frac{\mu_a}{D}}}{|\mathbf{r} - \mathbf{r}_s|^2} + \frac{1}{|\mathbf{r} - \mathbf{r}_s|^3}\right) \exp\left(\sqrt{\frac{\mu_a}{D}}|\mathbf{r} - \mathbf{r}_s|\right). \tag{13}$$

2.3 Radiance at a Detector in Fog

A solution to the RTE in (1) can be found by treating the in-scattering term as a source and integrating over the line of sight defined by distance R in Fig. 1.[20,21] Within a homogeneous medium and assuming no temporal variation ($\omega = 0$)

$$I(\mathbf{r}, \hat{\mathbf{\Omega}}) = \mu_s \int_0^\infty dR \exp\left[-(\mu_s + \mu_a)R\right] \int_{4\pi} d\hat{\mathbf{\Omega}}' f(\hat{\mathbf{\Omega}}' \to \hat{\mathbf{\Omega}}) I(\mathbf{r} - R\hat{\mathbf{\Omega}}, \hat{\mathbf{\Omega}}). \tag{14}$$

In this context $\hat{\mathbf{\Omega}}$ is directed towards a detector or pixel in fog. Considering Fig. 1, in-scattered light at positions $\mathbf{r} - R\hat{\mathbf{\Omega}}$ directed towards the pixel along the line of sight is attenuated and integrated at the detector. Assuming isotropic scatter ($f(\hat{\mathbf{\Omega}}' \to \hat{\mathbf{\Omega}}) = 1/4\pi$), we arrive at

$$I(\mathbf{r}, \hat{\mathbf{\Omega}}) = \frac{\mu_s}{4\pi} \int_0^\infty dR \exp\left[-(\mu_s + \mu_a)R\right] \phi(\mathbf{r} - R\hat{\mathbf{\Omega}}). \tag{15}$$

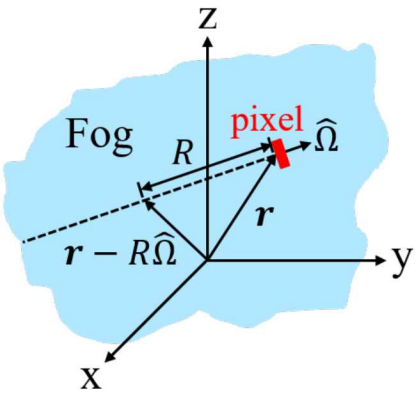

Figure 1. Coordinate system for calculating the radiance incident on a pixel at position $\mathbf{r}$ in fog. In-scattered light at positions $\mathbf{r} - R\hat{\mathbf{\Omega}}$ directed towards the pixel along the line of sight is attenuated and integrated at the detector according to (14).

Furthermore, assuming weak angular dependence from (3), we find that

$$I(\mathbf{r}, \hat{\mathbf{\Omega}}) = \frac{\mu_s}{4\pi} \int_0^\infty dR \exp\left[-(\mu_s + \mu_a)R\right] \left[\phi(\mathbf{r} - R\hat{\mathbf{\Omega}}) + 3g\mathbf{J}(\mathbf{r} - R\hat{\mathbf{\Omega}}) \cdot \hat{\mathbf{\Omega}}\right]. \tag{16}$$

Equation (16) contains an additional ansiotropic term compared to (15), and for the case of isotropic scatter ($g = 0$), reduces to (15), as expected. Combining (16) with (12) and (13) provides an analytic solutions for the light incident on a detector within a scattering media subject to the diffusion approximation to radiative transport. This solution is simulated in Section 3 with optical properties (μ_s, μ_a, and g) representative of fog, and compared to experiments in Section 6.

3. LIGHT PROPAGATION IN FOG

Interest at Sandia in characterizing and sensing in fog engendered the creation of one of the world's largest fog chambers in 2015 in Albuquerque, New Mexico.[25] At 3 x 3 x 55 m, the SNLFC provides a unique capability for sensor testing and the development of imaging methods in realistic and repeatable fog conditions. To characterize the fog, a transmissometer measures light attenuation and a particle sizer measures the size distribution of the water droplets.[19,26] This characterization of the fog is ideal for verification and validation of models that describe light transport in scattering media. In this section we present simulations of the spatial solutions (12) and (13) using the optical properties of the fog generated at the SNLFC.

3.1 Fog Optical Properties

Mie's solution to Maxwell's equations describes the scattering of a plane wave in a homogeneous medium by a sphere of known diameter and refractive index (RI).[27,28] The fields are written as an expansion in vector spherical harmonics, and coefficients describing the amplitudes of the scattered and internal fields can be calculated from the boundary conditions. The scattering and absorption efficiencies, Q_{sca} and Q_{abs}, as well as the anisotropy, g, can be written in terms of these coefficients. Assuming the spheres are far apart, $\mu_s = Q_{sca}An$ and $\mu_a = Q_{abs}An$, where $A = \pi(d/2)^2$ is the cross-sectional area of a sphere with diameter d, and n is the density of spheres (cm^{-3}). In fog, the spheres will have a distribution of diameters, d_i, where i denotes a parameter of the ith sphere. We

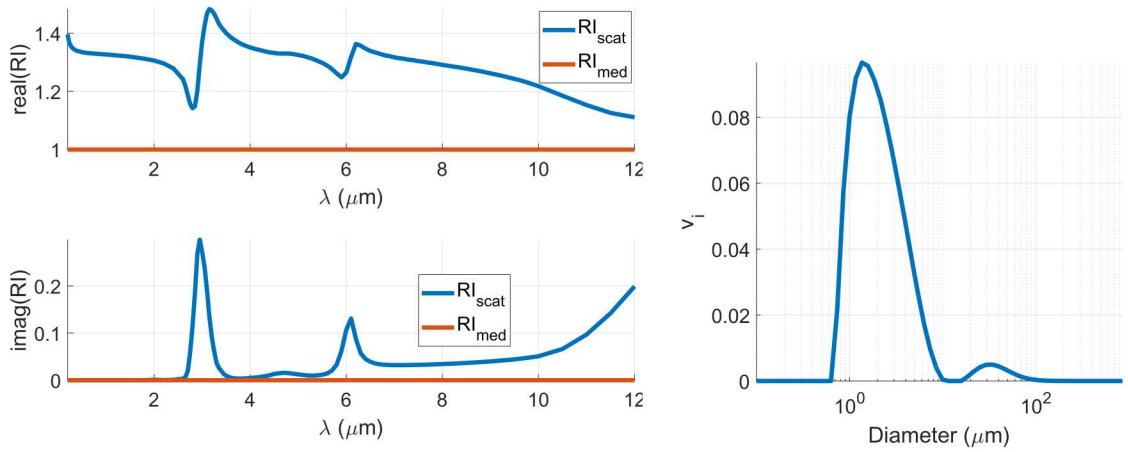

(a) (b)

Figure 2. Parameters used for simulation studies. (a) Real and imaginary parts of the refractive index (RI) of the scattering particle (water) and the background (free space). (b) Particle size distribution measured at the SNLFC.

then find that

$$\mu_s = \frac{3}{2} f_v \sum_i \frac{Q_{sca_i} v_i}{d_i} \tag{17}$$

$$\mu_a = \frac{3}{2} f_v \sum_i \frac{Q_{abs_i} v_i}{d_i} \tag{18}$$

$$\mu_s' = \frac{3}{2} f_v \sum_i \left(\frac{Q_{sca_i} v_i}{d_i} \right) (1 - g_i), \tag{19}$$

where f_v is the particle volume fraction and v_i is the percent of the total volume contributed by particles of diameter d_i. Experimentally, f_v and v_i can be determined from the transmissometer and particle sizer measurements at the SNLFC.[19]

We simulate fog optical properties using the RI and particle size distribution of Fig. 2. Figure 2(a) shows the real and imaginary parts of the RI of the sphere that is scattering light (water) and the background medium (assumed to be free space) as functions of wavelength λ. Figure 2(b) shows a particle size distribution measured at the SNLFC. Most particles have diameters less than 10 μm, which is typical of a radiation fog. Radiation fog commonly forms overnight above ground that is cooling by thermal radiation.[15] As the air temperature drops below the dew point, water vapor changes to a liquid state and forms microscopic spheres that remain suspended in the air due to collisions with gas molecules. The thermodynamics of the droplet formation is described by Köhler theory,[29] which allows prediction of droplet radius as a function of concentration of dissolved solute under conditions of supersaturation.[18]

Simulated optical properties from (17), (18), and (19), calculated for different fog particle densities n, are shown in Fig. 3. The averaged anisotropy g was computed as $g = 1 - \mu_s'/\mu_s$. As the wavelength is increased, the amount of scattering decreases, the light becomes less forward scattered, and the amount of absorption increases. Peaks in absorption corresponding to the resonances in Fig. 2(a) are observed at 2.95 μm and 6.1 μm. Two regions are found where $\mu_s > \mu_a$ and the diffusion approximation used to derive (5) applies. The first is at wavelengths between 200 nm and 2.7 μm, and the second is at wavelengths between 3.4 μm and 5.6μm. At wavelengths outside of these two regions, the diffusion approximation is expected to be insufficient to describe the light propagation.

3.2 Simulations

We use fog optical properties from Fig. 3 that are relevant to the experiment to simulate analytical solutions in Fig. 4. Light at $\lambda = 450$ nm and a fog density of 10^5 cm^{-3} were assumed, giving from Fig. 3, $\mu_s = 0.33$ m^{-1},

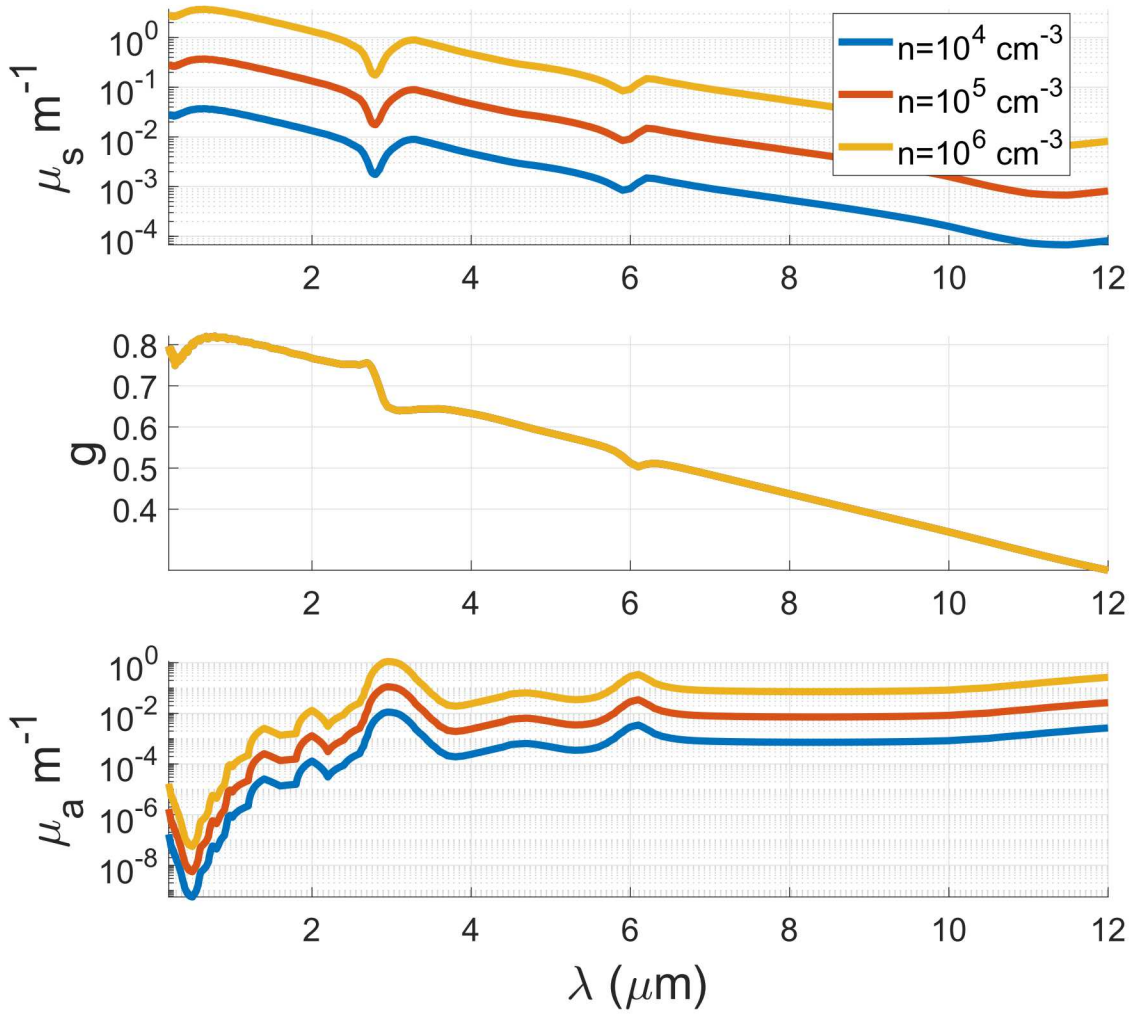

Figure 3. Fog optical properties simulated using Mie theory for different representative particle densities n using the parameters in Fig. 2.

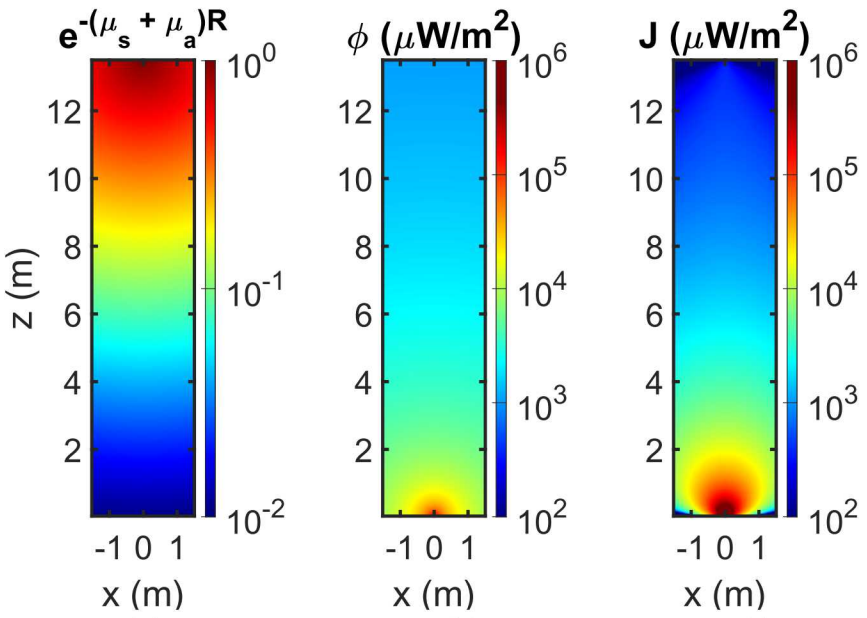

Figure 4. Light propagation simulations of spatial solutions using fog parameters and dimensions relevant to the experiment. An isotropic source is located at $\mathbf{r}_s = (0, 0, 0)$ m, and a detector is located at $\mathbf{r}_d = (0, 0, 13.5)$ m. A volume slice at $y = 0$ m is shown as an image. (a) Effect of extinction, where $R = |\mathbf{r}_d - \mathbf{r}|$ is distance to the detector, (b) Fluence rate from (12), and (c) Flux density from (13) in the direction of the detector. These three components allow calculation of the radiance at the detector using (16).

$g = 0.8$, and $\mu_a = 6.6 \times 10^{-9}$ m^{-1}. A 450 nm isotropic source is located at $\mathbf{r}_s = (x, y, z) = (0, 0, 0)$ m with $S_o = 2$ W. A detector is located at $\mathbf{r}_d = (0, 0, 13.5)$ m, and the simulation domain was discretized uniformly at 3 cm. The three components in Fig. 4(a), (b), and (c) contribute to the radiance at the detector according to (16).

4. CAMERA MEASUREMENT

Solving (16) with (12) and (13) requires that the line of sight for the detector is known. For a camera in fog, the line of sight of each pixel is defined by the imaging optics. We use the magnification principle to determine the positions of voxels in (x, y, z) space that are within the line of sight of a pixel in (x', y', z') space according to

$$x' = \frac{-d_i}{d_o - z} x = -Mx \tag{20}$$

$$y' = \frac{-d_i}{d_o - z} y = -My, \tag{21}$$

where d_i is the distance from the lens to the pixel array, d_o is the distance from the lens to the furthest point within the volume of interest, and M is the magnification of the lens. This type of problem can also be addressed experimentally using nonlinear calibration methods.[30]

5. EXPERIMENT

To validate the models developed in Sections 3.2 and 4, an experiment was performed at the SNLFC. A schematic showing the experimental setup is shown in Fig. 5. Details of the fog generation are described elsewhere.[18,19] Briefly, salt water solution was sprayed from 64 nozzles uniformly distributed along the length of the chamber. A Spraytec particle sizer from Malvern Instruments and a transmissometer provided the particle size distribution (v_i) and the particle density (n). The salt water was periodically sprayed in 25 minute cycles. During a cycle the fog density increases, and after the cycle is complete the fog density decreases. Throughout each cycle data was

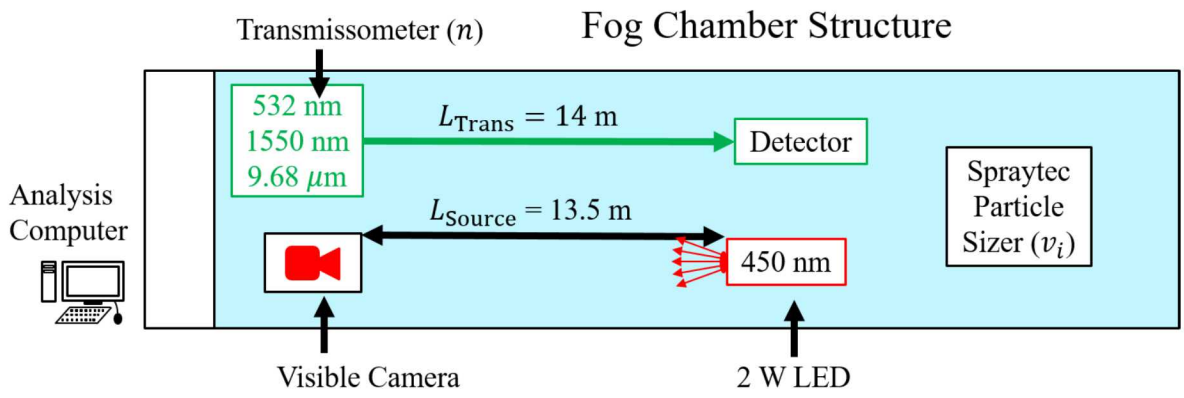

Figure 5. Experimental setup at the SNLFC. A three-band transmissometer at 0.532, 1.55, and 9.58 μm measures the light attenuation and a Spraytec particle sizer measures the particle size distribution. A visible camera is placed 13.5 m away from a 2 W LED emitting 450 nm light.

captured continuously by a visible CMOS camera (Basler acA2440) and the particle sizer and transmissometer, allowing camera images to be matched to the corresponding fog optical parameters μ_s, g, and μ_a using (17), (18), and (19). The light source was a 450 nm, 2 W mounted LED (Thorlabs M450LP1). The output of the LED was directed towards the camera, and assumed to approximate an isotropic source for the purposes of verifying (16). The distance between the LED and the camera was 13.5 m, nearly equivalent to the transmissometer distance, which may help account for any spatial variations in fog density n within the SNLFC.

6. RESULTS

Here we compare the experimental measurements to the model predictions. First, (20) and (21) were used with $d_i = 5$ cm and $d_o = 13.5$ m to determine the line of sight of each camera pixel. The camera was focused at infinity. The free-space projection of the pixel positions (x', y', z') into (x, y, z) space was tested using images of a resolution target at multiple depths, and the error was found to be less than 5%.

Images were captured using the experimental setup shown in Fig. 5 to compare to (16). The fog optical parameters μ_s, g, and μ_a were computed using (17), (18), and (19) and the transmissometer and particle sizer data. Representative results are presented in Fig. 6. The fog optical parameters μ_s' and μ_a are shown above the images in the left column. The plots to the right of each image compare measured data along the dashed white lines to the model predictions. The image counts were first converted to photons using the detector quantum efficiency and pixel saturation capacity. The photons measured by each pixel were then converted to energy (J), and finally to mW/m^2 using the detector integration time and the physical size of the pixel. The source power was not the same in each image; it was increased with fog density n to achieve sufficient signal at the pixels, and this was accounted for in the model. It was required to scale the experimental data by a constant value close to 1 so that the spatial variation of the model and data could be easily compared. Future work will include a calibration step to determine this constant scaling factor. The plots from left to right correspond to the dashed white lines from left to right, respectively. At low fog density, light scattered from the transmissometer is visible on the right in the images. We believe this scattered transmissometer light had a minimal impact on the results. To compare the measured and modeled data, we calculate the normalized mean square error (NMSE)[7]

$$\text{NMSE} = \left\{ \frac{\sum_{k=1}^{N} [P_i^{mod}(\mathbf{r}_{i_k}) - P_i^{exp}(\mathbf{r}_{i_k})]^2}{[P_i^{exp}(\mathbf{r}_{i_k})]^2} \right\}^{1/2}, \tag{22}$$

where $P_i^{mod}(\mathbf{r}_{i_k})$ is the model predicted pixel value, $P_i^{exp}(\mathbf{r}_{i_k})$ is the experimentally measured value, and k is an index from 1 to N of the pixel positions $\mathbf{r}_i$ used for the comparison.

In general, the model provides a very good prediction of the measured data. Considering the rows from top to bottom, the fog density n has increased by over an order of magnitude causing the image spatial profile

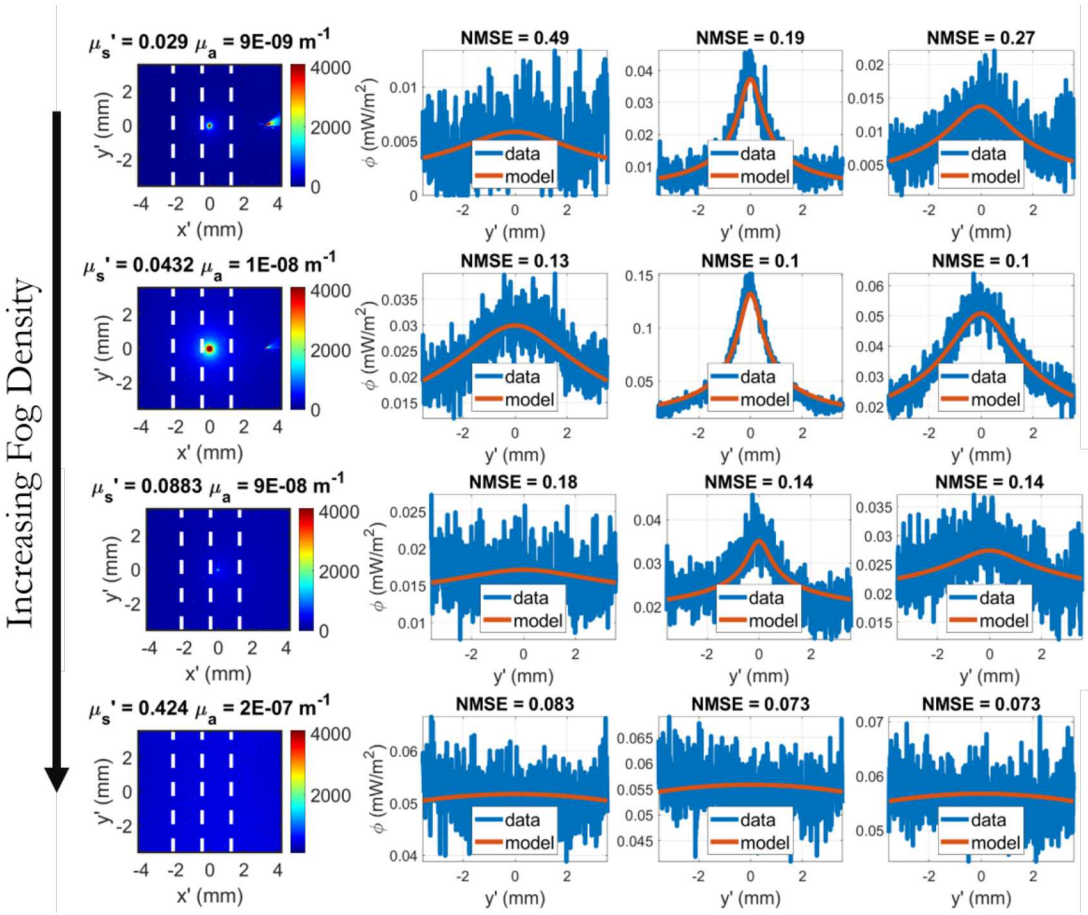

Figure 6. Modeling results using the DE's spatial analytical Green's function solutions demonstrated in Fig. 4(a) and (20) and (21) to determine the line of sight for each pixel.

to change significantly, and this is captured by the model. At low density, the mostly forward scattered light contributes to the peak in the radiance near the center of the image. Further away from the center of the image, light that is more highly scattered or diffuse contributes. At max density, only the highly scattered or diffuse glow is present with almost no spatial variation (the signal in the bottom image is well above the background).

Follow up simulations and experiments are planned to treat objects in fog. Numerical solutions based on the finite element method (FEM)[31] may be employed to better model sources, boundaries, and heterogeneous fog. These initial modeling and experimental results suggest that the diffusion approximation to the radiative transfer equation can predict the light propagation in fog. In future work, computational sensing and imaging methods will be explored that invert the models to enable detection, localization, and imaging of objects in fog for improved situational awareness.

Acknowledgment

This research was supported by the Laboratory Directed Research and Development (LDRD) Program at Sandia National Laboratories. We thank Laura J. Lemieux and Steven Storch for their assistance operating the Sandia National Laboratory Fog Chamber facility. We thank Philip L. Dreike for the useful discussions and for acting as program manager. Sandia National Laboratories is a multimission laboratory managed and operated by National Technology & Engineering Solutions of Sandia, LLC, a wholly owned subsidiary of Honeywell International Inc., for the U.S. Department of Energys National Nuclear Security Administration under contract DE-NA0003525. This paper describes objective technical results and analysis. Any subjective views or opinions that might be

expressed in the paper do not necessarily represent the views of the U.S. Department of Energy or the United States Government.

REFERENCES

[1] Mosk, A., Silberberg, Y., Webb, K., and Yang, C., "Imaging, sensing, and communication through highly scattering complex media," tech. rep., Defense Technical Information Center (2015).

[2] Gultepe, I., Pearson, G., Milbrandt, J., Hansen, B., Platnick, S., Taylor, P., Gordon, M., Oakley, J., and Cober, S., "The fog remote sensing and modeling field project," *Bulletin of the American Meteorological Society* **90**(3), 341–360 (2009).

[3] Fultz, A. J. and Ashley, W. S., "Fatal weather-related general aviation accidents in the United States," *Physical Geography* **37**(5), 291–312 (2016).

[4] Ashley, W. S., Strader, S., Dziubla, D. C., and Haberlie, A., "Driving blind: Weather-related vision hazards and fatal motor vehicle crashes," *Bulletin of the American Meteorological Society* **96**(5), 755–778 (2015).

[5] Pisano, P. A., Goodwin, L. C., and Rossetti, M. A., "US highway crashes in adverse road weather conditions," in [*24th Conference on International Interactive Information and Processing Systems for Meteorology, Oceanography and Hydrology, New Orleans, LA*], (2008).

[6] Chandrasekhar, S., [*Radiative Transfer*], Courier Corporation (1960).

[7] Ye, J. C., Webb, K. J., Bouman, C. A., and Millane, R. P., "Optical diffusion tomography by iterative-coordinate-descent optimization in a Bayesian framework," *Journal of the Optical Society of America A* **16**(10), 2400–2412 (1999).

[8] Arridge, S. R., "Optical tomography in medical imaging," *Inverse Problems* **15**, R41–R93 (1999).

[9] Bentz, B. Z., Lin, D., Patel, J. A., and Webb, K. J., "Multiresolution localization with temporal scanning for super-resolution diffuse optical imaging of fluorescence," *IEEE Transactions on Image Processing* (2019).

[10] Bentz, B. Z., Wu, T. C., Gaind, V., and Webb, K. J., "Diffuse optical localization of blood vessels and 3D printing for guiding oral surgery," *Applied Optics* **56**(23), 6649–6654 (2017).

[11] Bentz, B. Z., Lin, D., and Webb, K. J., "Superresolution diffuse optical imaging by localization of fluorescence," *Physical Review Applied* **10**(3), 034021 (2018).

[12] Bentz, B. Z., Mahalingam, S. M., Ysselstein, D., Montenegro, P. C., Cannon, J. R., Rochet, J.-C., Low, P. S., and Webb, K. J., "Localization of fluorescent targets in deep tissue with expanded beam illumination for studies of cancer and the brain," *IEEE Transactions on Medical Imaging* (2020).

[13] Tsai, E. H., Bentz, B. Z., Chelvam, V., Gaind, V., Webb, K. J., and Low, P. S., "In vivo mouse fluorescence imaging for folate-targeted delivery and release kinetics," *Biomedical Optics Express* **5**(8), 2662–2678 (2014).

[14] Bentz, B. Z., Chavan, A. V., Lin, D., Tsai, E. H., and Webb, K. J., "Fabrication and application of heterogeneous printed mouse phantoms for whole animal optical imaging," *Applied Optics* **55**(2), 280–287 (2016).

[15] van der Laan, J. D., Wright, J. B., Kemme, S. A., and Scrymgeour, D. A., "Superior signal persistence of circularly polarized light in polydisperse, real-world fog environments," *Applied Optics* **57**(19), 5464–5473 (2018).

[16] van der Laan, J. D., Wright, J. B., Scrymgeour, D. A., Kemme, S. A., and Dereniak, E. L., "Evolution of circular and linear polarization in scattering environments," *Optics Express* **23**(25), 31874–31888 (2015).

[17] van der Laan, J. D., Wright, J. B., Scrymgeour, D. A., Kemme, S. A., and Dereniak, E. L., "Effects of collection geometry variations on linear and circular polarization persistence in both isotropic-scattering and forward-scattering environments," *Applied Optics* **55**(32), 9042–9048 (2016).

[18] Wright, J. B., van der Laan, J. D., Sanchez, A., Kemme, S. A., and Scrymgeour, D. A., "Optical characterization of the Sandia fog facility," in [*Degraded Environments: Sensing, Processing, and Display 2017*], **10197**, 1019704, International Society for Optics and Photonics (2017).

[19] Redman, B. J., van der Laan, J. D., Westlake, K. R., Segal, J. W., LaCasse, C. F., Sanchez, A. L., and Wright, J. B., "Measuring resolution degradation of long-wavelength infrared imagery in fog," *Optical Engineering* **58**(5), 051806 (2019).

[20] Bell, G. I. and Glasstone, S., "Nuclear reactor theory," tech. rep., US Atomic Energy Commission, Washington, DC (United States) (1970).

[21] Duderstadt, J. J. and Hamilton, L. J., [*Nuclear Reactor Analysis*], Ann Arbor, Michigan: Wiley-Interscience (1976).

[22] Haskell, R. C., Svaasand, L. O., Tsay, T.-T., Feng, T.-C., McAdams, M. S., and Tromberg, B. J., "Boundary conditions for the diffusion equation in radiative transfer," *Journal of the Optical Society of America A* **11**(10), 2727–2741 (1994).

[23] Patterson, M. S., Chance, B., and Wilson, B. C., "Time resolved reflectance and transmittance for the noninvasive measurement of tissue optical properties," *Applied Optics* **28**(12), 2331–2336 (1989).

[24] Ripoll, J., Nieto-Vesperinas, M., and Carminati, R., "Spatial resolution of diffuse photon density waves," *Journal of the Optical Society of America A* **16**(6), 1466–1476 (1999).

[25] Clark, H., "Fog on demand: Sandia-operated facility makes testing optics more cost-effective, efficient," *Sanida Lab news* (2015).

[26] Glen, A. and Brooks, S. D., "Single particle measurements of the optical properties of small ice crystals and heterogeneous ice nuclei," *Aerosol Science and Technology* **48**(11), 1123–1132 (2014).

[27] Bohren, C. F. and Huffman, D. R., [*Absorption and scattering of light by small particles*], John Wiley & Sons (2008).

[28] Bentz, B. Z., Bowen, A. G., Lin, D., Ysselstein, D., Huston, D. H., Rochet, J.-C., and Webb, K. J., "Printed optics: phantoms for quantitative deep tissue fluorescence imaging," *Optics Letters* **41**(22), 5230–5233 (2016).

[29] Köhler, H., "The nucleus in and the growth of hygroscopic droplets," *Transactions of the Faraday Society* **32**, 1152–1161 (1936).

[30] Soloff, S. M., Adrian, R. J., and Liu, Z.-C., "Distortion compensation for generalized stereoscopic particle image velocimetry," *Measurement Science and Technology* **8**(12), 1441 (1997).

[31] Schweiger, M. and Arridge, S. R., "The Toast++ software suite for forward and inverse modeling in optical tomography," *Journal of Biomedical Optics* **19**(4), 040801 (2014).